Applied Physics Reviews

Core–sheath polymer nanofiber formation by the simultaneous application of rotation and pressure in a novel purpose-designed vessel

Cite as: Appl. Phys. Rev. **8**, 041412 (2021); https://doi.org/10.1063/5.0071257
Submitted: 13 September 2021 • Accepted: 08 November 2021 • Published Online: 01 December 2021

Hussain Alenezi, Muhammet Emin Cam and Mohan Edirisinghe

Applied Physics Reviews ARTICLE scitation.org/journal/are

Core–sheath polymer nanofiber formation by the simultaneous application of rotation and pressure in a novel purpose-designed vessel

Cite as: Appl. Phys. Rev. 8, 041412 (2021); doi: 10.1063/5.0071257
Submitted: 13 September 2021 · Accepted: 8 November 2021 ·
Published Online: 1 December 2021

Hussain Alenezi,[1,2] Muhammet Emin Cam,[3,4] and Mohan Edirisinghe[1,a)]

AFFILIATIONS

[1]Department of Mechanical Engineering, University College London, Torrington Place, London WC1E 7JE, United Kingdom
[2]Department of Manufacturing Engineering, College of Technological Studies, PAAET, 13092 Kuwait City, Kuwait
[3]Center for Nanotechnology and Biomaterials Application and Research, Marmara University, Istanbul 34722, Turkey
[4]Department of Pharmacology, Faculty of Pharmacy, Marmara University, Istanbul 34854, Turkey

[a)]Author to whom correspondence should be addressed: m.edirisinghe@ucl.ac.uk

ABSTRACT

Forming polymeric core–sheath nanofibers is gaining prominence owing to their numerous potential applications, most notably in functional scenarios such as antiviral filtration, which is attracting significant attention due to the current COVID pandemic. This study has successfully designed and constructed a novel pressurized gyration vessel to fabricate core–sheath polymer nanofibers. Several water-soluble and water-insoluble polymer combinations are investigated. Both polyethylene oxide and polyvinyl alcohol were used as the core while both poly(lactic acid) (PLA) and poly(caprolactone) (PCL) were used as the sheath; PLA and PCL were used as core and sheath, in different instances; respectively. The fluid behavior of the core–sheath within the vessel was studied with and without applied pressure using computational fluid dynamics to simulate the core–sheath flow within the chamber. A high-speed camera was used to observe the behavior of jetted solutions at core–sheath openings, and the best scenario was achieved using 6000 rpm spinning speed with 0.2 MPa (twice atmospheric) applied pressure. The surface morphology of core–sheath fibers was studied using a scanning electron microscope, and focused ion beam milling assisted scanning electron microscopy was used to investigate the cross-sectional features of the produced fibers. Laser confocal scanning microscopy was also used to verify the core–sheath structure of the fibers, which were further characterized by Fourier transform infrared spectroscopy and differential scanning calorimetry. Thus, using a variety of polymer combinations, we show, both theoretically and experimentally, how core–sheath fibers evolve in a vessel that can serve as a scalable manufacturing pressurized gyration production process.

I. INTRODUCTION

Polymeric nanofibers possess a diameter of less than 1000 nm.[1] Nanofibers have attracted tremendous attention due to their spectacular features in a broad spectrum of research and commercial applications, especially biomedical engineering, energy generation and storage, chemical and biological sensors, water purification, and environmental remediation.[2] Nanofibers of some polymers can also show nontoxic biodegradability and biocompatibility. One of the other most remarkable properties of nanofibers is their extremely high surface area-to-volume ratio and surface porosity, which makes them an attractive and robust product for many advanced healthcare applications.[3] However, if we are able to mass-produce nanofibers with a core–sheath structure, it will immensely help accelerate their usage in these high technology applications as the key functional property can be concentrated on the surface regions (sheath) while the core mainly provides mechanical support. Achieving this at the nanoscale is the main aim of this paper.

Nanofibers can be fabricated from various basic materials, including synthetic polymers, natural polymers, semiconducting materials, carbon-based materials, and composite materials. In this work we focus on polymeric materials. Polyvinyl alcohol (PVA), polyvinylpyrrolidone (PVP), and polyethylene oxide (PEO) are the most popular water-soluble, extremely low cytotoxic, biocompatible, and biodegradable synthetic polymers.[4]

On the other hand, poly(lactic acid) (PLA), poly(lactic-co-glycolic acid) (PLGA), and poly(caprolactone) (PCL) are among the well-documented Food & Drug Administration (FDA)-approved polymers widely used to prepare drug delivery systems.[5]

Bicomponent micro/nanofibers have been widely investigated in the past few decades. They are novel products composed of either thermoplastic or thermoset polymers. These products have advantages depending on the characteristics of the polymers, such as their physical, mechanical, or chemical features.[6] Bicomponent nanofibers are majorly created in the desired structure, such as core/sheath, side by side, and islands in the sea.[7] Core–sheath is the most preferred configuration for bicomponent fibers. In core–sheath nanofibers, the core can even be composed of carbon nanotube (CNT), nanoclay, silver nanoparticles, and be covered by another material such as polymers. Especially in healthcare, core–sheath nanofibers can be used as tissue engineering scaffolds, drug delivery media, and wound dressings.[8,9] One of the most important applications of core–sheath nanofibers is the encapsulation of drugs for gene therapy, reinforcement, drug delivery, self-healing, and tissue engineering.[10,11] Several crucial reasons for fabricating core–sheath structures include separating and surrounding the core from a volatile environment, controlling and increasing the drug release time, mimicking the natural extracellular matrix for tissue engineering and regeneration, and increasing the mechanical strength of the products.[12]

New production methods are frequently needed to accompany the evolution of core–sheath nanofibers and their demand in an increasing number of applications.[13] In these developments, basically, two different polymer solutions meet at the outlet of the spinneret with different cross sections to make the desired configuration.[14] Such structures can be produced using different techniques, e.g., coaxial melt spinning[15,16] and electrospinning.[17] These techniques are pioneering and useful but do have some limitations, such as material selection restrictions and yield.[18]

Pressurized gyration (PG), developed in 2013, exploits a selected polymer solution's Rayleigh–Taylor instability, and is based on the simultaneous application of rotation speed and pressure.[19,20] When gyration via a motor begins, the rotational speed rapidly rises, resulting in a greater centrifugal force. The polymer solution is displaced as a result of the increased force. This causes a pressure difference inside the vessel due to the applied gas pressure interacting with the liquid, forcing the solution out. Due to the differential in the surface tension on the liquid–air interface, the centrifugal force is the primary driver of liquid extrusion through the formed vessel holes. This gradient induces tangential Marangoni stress at the liquid–gas interface, thus initiating flow at the polymer droplet tip.[21–23] By continually stretching the polymer jet as it exits the holes, the centrifugal force creates fibers. Also, pressure difference is produced by the gas inlet situated at the holes. Evaporation steadily causes solvent loss, and the fiber source strand is the ejected polymer that remains in the flow. The dried fiber ultimately precipitates on the collecting walls, and the fast repeating of this operation creates a bundle of fibers.[24]

Centrifugal spinning (CS) and PG, and their operating conditions have been investigated by researchers worldwide to manufacture nanoscale fibers. The use of numerical modeling, such as computational fluid dynamics (CFD), provides many advantages for studying the fluid behavior of polymer fluids throughout manufacturing applications,[25] resulting in the best scenario with the least waste, though, due to the particular use of experimental techniques, this approach is not always feasible. In order to simulate PG and CS processes, the following primary factors are taken into account: air drag, centrifugal force, Coriolis force, spinning speed, polymer viscosity, and solvent evaporation time in the collector during the spinning process for both processes, and the applied pressure for only PG.[26–28] Recently, core–sheath microstructure forming has been extensively reviewed by Mahalingam *et al.*[29] Although electrospinning can form core–sheath structures, for scaled up manufacturing it is not ideal, compared to pressurized gyration, which can be translated from laboratory to reality by making manufacturing-friendly vessels as shown in this paper. In addition, few studies have been conducted to prepare and optimize the morphology of core–sheath polymeric fibers using simulation and modeling[30] and, overall, there is a dearth of research on fabrication techniques for core–sheath manufacturing because of the complicated nature of the forming procedure.[31] This paper aims to fill that gap. In earlier work, Edirisinghe and co-workers[32–34] used a simple laboratory pot to show how core–sheath structures can be formed using pressurized gyration. It must be stressed that this work uses a specially designed scalable vessel (illustrated in Fig. 1) and delivers a seismic change to the scalable mass production of core–sheath fibers, where the size distribution mean sits in the nanoscale.

In this study, a novel core–sheath vessel was designed and constructed to fabricate polymeric core–sheath nanofibers using water-soluble polymers such as PEO and PVA, as core. In contrast, water-insoluble polymers such as PLA and PCL were used as sheath. We also used the latter in both core and sheath combinations. Furthermore, CFD was utilized to validate the flow in the novel purpose-designed vessel by studying the fluid behavior of the polymeric solutions within the core–sheath reservoirs and optimizing the best scenario for spin speed in CS and the pressure applied in PG techniques. In addition, a high-speed camera was used to observe the fluid behavior of the jetted polymer solution from the core and sheath openings to optimize the best process scenarios by varying the spinning speeds and the use of applied pressure. Furthermore, the external morphology, fiber diameter, cross-sectional structure, fluorescence images, microstructure, and thermal properties of produced core–sheath fibers were analyzed. This study shows the importance of the simultaneous application of pressure and rotation to form core–sheath fibers at specific conditions, for mass production.

II. MATERIALS AND METHODS

A. Materials

In this investigation, stainless steel (Grade-316), clear polycarbonate (PC), and Teflon were used to design and fabricate the reservoirs and other parts of the vessel are described in Sec. II C. The water-soluble polymers used were polyethylene oxide (PEO) (Mw 6×10^5 g mol^{-1}) and polyvinyl alcohol (PVA) (Mw: 89 000–98 000 g mol^{-1}). In addition, poly (L-lactic acid) (PLA, Mw: 110 000 g mol^{-1}) and poly (caprolactone) (PCL, Mw ~80 000) water-insoluble polymers were used in this study. Distilled water was used to dissolve the PEO and PVA, while chloroform and methanol were used for PLA and PCL. All polymers and color dyes (Rhodamine and Uranine) were purchased from Sigma Aldrich (Poole, UK); all purchased reagents were of analytical grade.

B. Solution preparation and characterization

PEO and PVA were completely dissolved at concentrations 10 and 20 wt. %, respectively, in de-ionized water while PCL and PLA

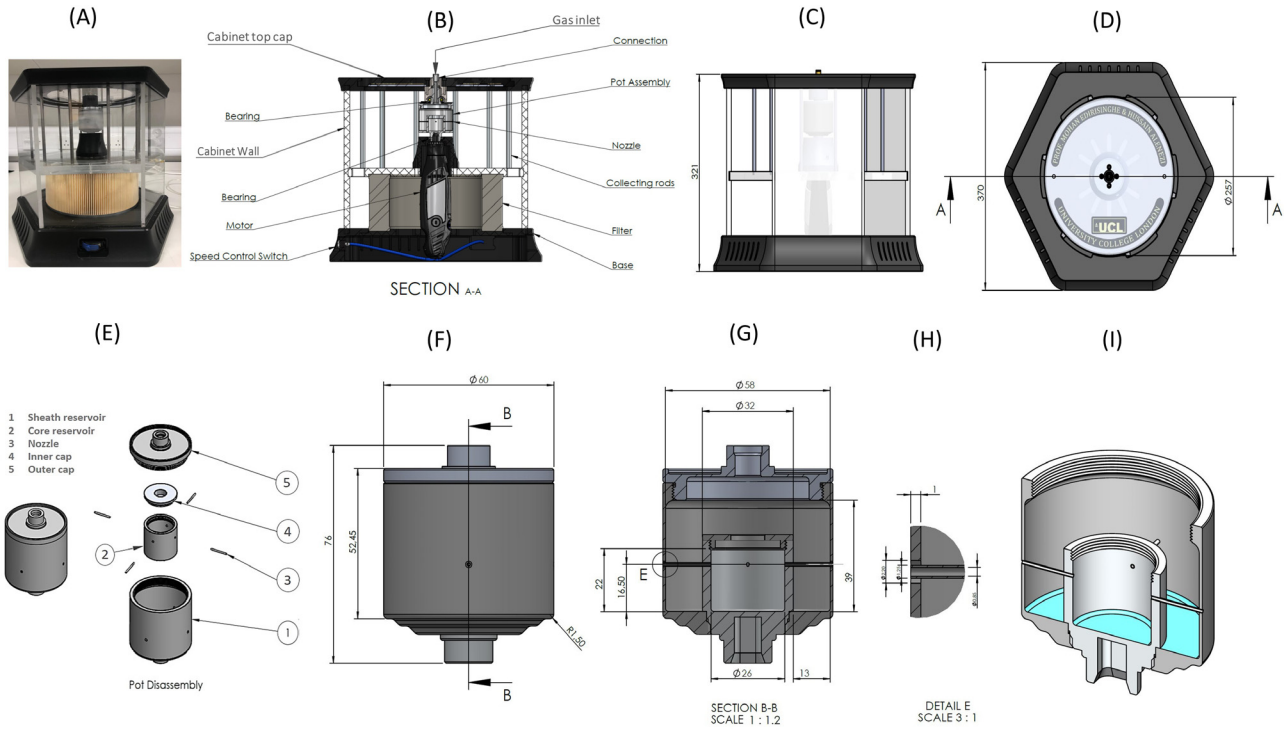

FIG. 1. Main parts of the vessel: (a) full view, (b) cross-sectional view for device parts, showing (c) height, (d) width, (e) core–sheath reservoir disassembled, (f) reservoir external dimensions, (g) reservoir internal dimensions, (h) orifices dimensions, and (i) reservoir cross-sectional side view.

were completely dissolved at concentration 20 wt. % into a mixture of chloroform and methanol in ratio 3:1, v/v. The polymer solutions were stirred magnetically for 24 h and kept at ambient/room temperature (∼25 °C). For fluorescence staining, the core solution was mixed with Rhodamine B powder fluorescent dye (red color) (20 mg/10 ml) while the sheath solution was mixed at the same ratio with Uranine (green color); all these solutions were stirred for 2 h before using PG. Parameters such as density, viscosity, and surface tension for the solutions were measured using a regular 10 ml density bottle; DIN ISO 3507-Gay-Lussac (Boru Cam Inc., Republic of Turkey); a viscometer (Brookfield DV-111, Harlow, UK); and a force tensiometer (Kruss K9, Hamburg, Germany), respectively. All the measurements were repeated three times at ambient temperature. These equipments were calibrated prior to measurements.

C. Device design and construction

Figure 1(a) illustrates the novel portable core–sheath vessel used in this investigation. The device can be divided into three main parts: first, the cabinet with hexagonal shape has 321 mm height and 370 width consists of parts illustrated in [Fig. 1(b)], which shows all vessel parts in a cross-sectional view to illustrate the device skeleton. Second, the novel core–sheath reservoirs, as shown in Figs. 1(e)–1(i), demonstrate the design of the dual cylindrical reservoirs. It consists of a core chamber placed at the center of the sheath vessel, with an internal diameter of 26 mm, a height of 22 mm, and a thickness of 3 mm and fitted with a hallow screw cap with 32 mm outer, 12 mm inner diameter, and a height of 5 mm. Four holes with 1.25 mm diameter were symmetrically placed at 90° at 16.5 mm height to locate the nozzles. Four nozzles with 1.25 mm and 0.85 mm external and internal diameters, respectively, and 17 mm in length were placed from the inner edge of the core reservoir to the external edge of the sheath chamber as shown in Figs. 1(g) and 1(h). Thus, the sheath reservoir has a 60 mm outer diameter, 13 mm internal space from the core chamber, a 39 mm internal height, and four holes with a 2.2 mm diameter positioned at the exact center of the core chamber. A screw cap was attached to the sheath reservoir at the topside with 60 and 5.2 mm outer and inner diameters, respectively, to fit the rotary union to infuse gas pressure. To ensure the pot fitted correctly to the top cabinet side fixture and the DC motor, the top and bottom sides of the reservoir were attached to fitted bearings, as shown in Fig. 1(b), to reduce the vibration, centralize the core–sheath chamber, and use the vessel safely. Three cabinet walls unite the topside with the device's base of 14 mm thickness connected to the middle base part of 25 mm thickness, which permits aerodynamics inside the device.

Twelve collector rods made from stainless steel (316) with 6 mm diameter and 145 mm length are fixed in the middle and the top base. Finally, the reservoir is linked to a high-speed DC motor allowing up to 35 000 rpm. It is fixed on a Teflon base at the center of the vessel and controlled by a speed control switch mounted on the vessel base with an ON/OFF switch. The materials and tools used in the manufacturing process give numerous advantages, including its small size, low weight (3.6 kg), and ease of use, therefore, making it quite portable.

D. High-speed camera imaging

The behavior of the polymer solutions in the core and the sheath spurted out from the reservoirs was observed using high-speed camera (Photron, FASTCAM SA1.1 model 675-M2, Tokyo, Japan) imaging, which captured 5400 and 20 000 frames per second.

E. Design of experiments

In this investigation, the core chamber was loaded manually with 2 ml of core polymer solution, while the sheath chamber was loaded with 3 ml solution using a syringe. Various spinning speeds from 2000 to 10 000 rpm were used to observe the optimum jetted core, sheath, and core–sheath fibers. Nitrogen gas was infused inside the chambers at 0.1, 0.2, and 0.3 MPa during PG and gas was not used in the CS scenario. A tachometer was used to calibrate the pot spinning speed; the total experiment time was 180 s. The optimum spinning speed for the CS scenario was 6000 rpm, whereas for the PG scenarios, it ranged from 6000 to 8000 rpm. To observe the fluid behavior of the jetted polymer solutions from the core, sheath, and core–sheath, polyethylene oxide (PEO) was used in the polycarbonate core–sheath reservoir. For the rest of the data collected in this study, stainless steel reservoirs were used to prevent any damage caused by the solvents.

F. Numerical study

Numerical simulations of core–sheath fluids and gas within the cylinder were developed using a CFD package (ANSYS-Fluent 19) to investigate the fluid behavior inside reservoirs and jetted liquids in order to verify the new core–sheath reservoir design prior to fiber forming. The effect of rotation speed and gas pressure was studied. The governing equations for the flow, volume fractions, and pressure values were solved for each cell in the three phases. The initial stage was to use solidworks to build a three-dimensional (3D) geometrical model of the core–sheath study, as shown in Fig. 2. The second step was to generate a mesh. The method and boundary conditions were defined as the last stage. For this study, we used a pressure-based transient-state solver. The number of iterations was permitted to increase until the converged solution of continuity, energy, velocity, turbulence, and momentum was obtained. Interaction of the three phases of core–sheath solutions and gas was modeled as a multi-phase model, whereas the finite volume method was used to govern the equations and for pairing pressure–velocity a simple algorithm was required. The first-order upwinding scheme was mainly responsible for discrete convection terms such as momentum, energy, and turbulent kinetic energy equations. Therefore, under-relaxation factors of 0.01, 0.8, 0.8, and 1.0 were used for momentum, turbulent kinetic energy, turbulent dissipation rate, and turbulent viscosity, respectively.

1. Rotating core–sheath reservoirs

In the spinning cylinders, both core–sheath reservoirs were filled with 5 mm (height) of PEO solution, including instances when nitrogen gas was loaded into the reservoirs. As a result, the fluid starts at rest at the bottom of both cylinders. In addition, the filled fluids for the core and sheath start at rest from the bottom side of the reservoir, then start spinning at a constant speed. These assumptions provide the following Navier–Stokes equations of motion for a curved liquid jet in the inviscid and viscous cases as follows:

$$\nabla \mathrm{u}^{\rightarrow} = 0, \tag{1}$$

$$\frac{\partial \vec{u}}{\partial \mathrm{t}} + (\vec{u}\cdot\nabla)\vec{u} = -\frac{1}{\rho}\nabla \mathrm{p} + \frac{\mu}{\rho}\nabla^2\vec{u} - 2\vec{\omega}\times\vec{u} - \vec{\omega}\times(\vec{\omega}\times\vec{r}), \tag{2}$$

where u, p, μ, and ρ are the velocity, the pressure, the viscosity, and the density of the jet, respectively; ω is the angular velocity of the vessel, r is the position vector in the rotating frame, and t is the time.

The instability between the PEO and the gas interface could be specified by equating the disrupting gravitational force per unit volume to the stabilizing surface tension force per unit volume as follows:

$$\rho g \frac{\partial h}{\partial x} = \gamma \frac{\partial^3 h}{\partial^3 x}, \tag{3}$$

ρ is the density of the polymer solution, g is the gravitational force, γ is the PEO–gas surface tension, h is the height of the PEO drop suspended under the horizontal surface, and x is the vertical distance.

2. Turbulence model

A realizable k–ε turbulence model was employed to simulate the turbulent flow. Transport equations for the turbulent kinetic energy

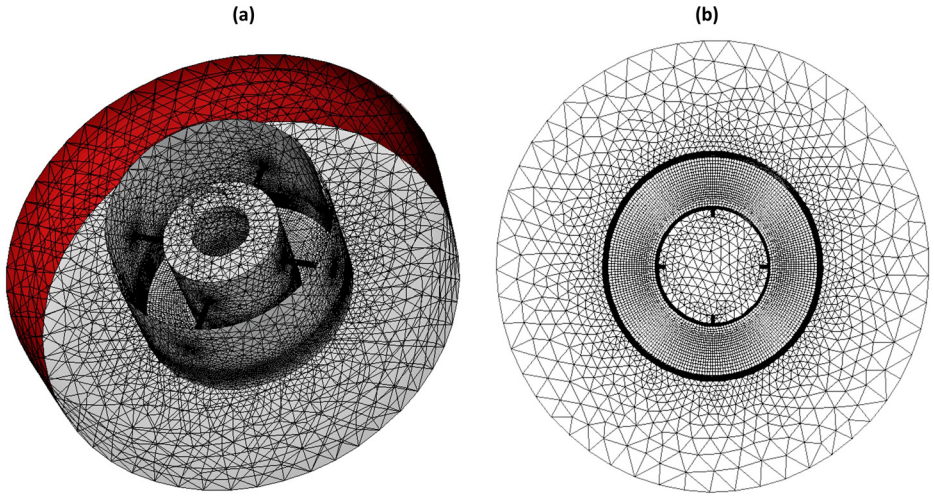

FIG. 2. Grid system for the core–sheath reservoir: (a) 3D full domain and (b) bottom view of the domain.

and its dissipation rate were used with standard wall functions. The adopted model meets the accuracy and reliability requirements in the considered fluid flow study.

The turbulent kinetic energy k equation is given by

$$\frac{\partial}{\partial t}(\rho k) + \frac{\partial}{\partial x_i}(\rho k u_j) = \frac{\partial}{\partial x_i}\left[\left(\mu + \frac{\mu_t}{\sigma_k}\right)\frac{\partial k}{\partial x_j}\right] + G_k + G_b - \rho\epsilon - Y_M + S_k, \quad (4)$$

and the turbulent kinetic energy ε equation is given by

$$\frac{\partial}{\partial t}(\rho \varepsilon) + \frac{\partial}{\partial x_j}(\rho \varepsilon u_j) = \frac{\partial}{\partial x_j}\left[\left(\mu + \frac{\mu_t}{\sigma_\epsilon}\right)\frac{\partial \epsilon}{\partial x_j}\right] + \rho C_1 S_\epsilon - \rho C_2 \frac{\epsilon^2}{K + \sqrt{\nu\epsilon}} + C_{1\epsilon}\frac{\epsilon}{K} C_{3\epsilon} G_b + S_\epsilon, \quad (5)$$

where

$$\mu_{t=\rho c_\mu}\frac{k^2}{\varepsilon},\ C_1 = \max\left[0.43, \frac{\eta}{\eta+5}\right],\ \text{and}\ \eta = S\frac{k}{\epsilon}, \quad (6)$$

where

$$G_k = \mu_t\left(\frac{\partial u_i}{\partial x_j} + \frac{\partial u_j}{\partial x_i}\right)\frac{\partial u_i}{\partial x_j}. \quad (7)$$

G_k and G_b are generations of turbulence kinetic energy due to the mean velocity gradients and buoyancy, respectively. The contribution of the actuating dilatation in compressible turbulence to the overall dissipation rate is (Y_M), whereas σ_k and σ_ϵ are the turbulent Prandtl numbers for k and ε, respectively; S_k and S_ε are user-defined source terms and μ_t and μ are the eddy and dynamic viscosity, respectively.

The empirical constants for the realizable k–ε model were assigned[35–38] as follows:

$$C_\mu = 0.09,\ C_{1\varepsilon} = 1.44, C_2 = 1.92, \sigma_k = 1.0,\ \text{and}\ \sigma_\epsilon = 1.2.$$

This research utilized a first-order implicit scheme and a simple scheme for pressure-speed coupling with spatial discretization. In addition, there were also cell-based least squares schemes for the gradient, presto schemes for pressure, geo-reconstruct schemes for volume fractions, and a first-order upwind method for turbulent kinetic energy, in addition to other methods that were applied.

3. Mesh generation

Due to the intricacy of the model, unstructured grids were used for the computational domain. Mesh refinements were used in the area close to the walls, as illustrated in Fig. 2. Grid-dependency is checked for three distinct grids—689 251, 795 682, and 985 621 cells—to verify the grid's solution independence. It indicated that there is no difference in the results between the second and the third configurations; therefore, 795 682 was chosen for the simulation, standard curvature meshes generated by CFD software (FLUENT) were utilized.

4. Initial conditions

The core and sheath reservoirs were filled with PEO solution to a height of 5 mm from the bottom for all simulation tests, and the cylinder was assumed to spin at a constant speed to shorten the processing time. Additionally, it was apparent that the cylinder's rotation must remain constant at the highest speed to study the effect of nitrogen gas pressure. For both solutions, the surface tension was assigned as 0.1564 N m^{-1} (see Sec. III A below).

5. Boundary conditions

The ambient temperature was fixed at 25 °C, and the pressure was set at 0.2 MPa to investigate the impact of gravitational force. Spinning speed (ω = 6000 rpm) was used without applying nitrogen gas in the CS scenario; the gas pressure used in the simulations was 0.2 MPa in PG at the same speed. A 10 mm diameter hole at the middle of the top of the core–sheath chamber served as the gas intake.

G. Characterization of core–sheath fibers

1. Scanning electron microscope (SEM)

The morphologies of all fibers were examined with SEM (EVO LS 10, ZEISS SEM instrument). Before imaging, the surface of samples was coated with gold (Au) approximately for 60 s with a sputter coating machine (Quorum SC7620, ABD). The applied accelerating voltage was 10 kV, and the working distance was 23 mm. Subsequently, the average fiber diameter and distribution were analyzed using ImageJ (Brocken Symmetry Software).

2. Focused ion beam (FIB)

The polymeric fiber samples were gold (Au) coated for 60 s at 10 mA current utilizing the sputter coating method due to their nonconductive nature. Hitachi NX5000 Focused Ion and Electron Beam System (FIB) was employed for precisely cutting and imaging the samples. Since the polymeric fibers have low melting points, core–sheath fiber samples were chosen to be coarser and singular to prevent any distortion on the cross-sectional surface, during the etching process in FIB-SEM. With respect to the much smaller nanofibers, it was difficult to preserve these during FIB. In addition, the cold-field emission electron gun, gas injection system, upper and lower secondary electron detector (USED and LSED) features were used. To prevent single fiber bending during cutting and imaging with an ion beam, tungsten (W) was spot-welded to the fiber by using the ion deposition process and gas injection system of the FIB. At this stage, single frame imaging (view mode, 10 pA) was performed using an ion beam, while welding was performed in ultrafine (100 pA) and fine (280 pA) modes to prevent sample damage and bending. Furthermore, FIB's focused ion milling (FIM) feature cut the remaining single fibers. Then, the beam was used to cut single fibers at 30 kV, rough (12 nA), fine (280 pA), and ultrafine (100 pA). The slicing method has been employed to have a smooth and clean cut, particularly in the ultrafine setting. After cutting, samples were observed with USED and LSED at 5 kV accelerating voltage and 20 uA probe current, with samples inclined 54° to examine cross sections.

3. Fourier transform infrared spectroscopy (FTIR)

Utilizing FTIR (Jasco FTIR 4700 spectrometer), the interactions between all the components used in the fiber manufacturing process and the chemical structures of these components were examined at

room temperature between 4000 and 400 cm^{-1}. These studies were performed with 32 scans with 4 cm^{-1} resolutions. OPUS Viewer version 6.5 was used to analyze the spectra.

4. Differential scanning calorimeter (DSC)

The thermal properties of the fibers were determined by DSC (Perkin Elmer Jade DSC) and Pyres software (PerkinElmer Inc., MA, USA) under a dynamic argon atmosphere (20 ml min^{-1}) in the heating range of 0–350 °C at a heating rate of 10 °C min^{-1}. Temperature calibration of DSC was performed according to the indium melting point and melting enthalpy. Perkin Elmer aluminum sample pans and covers were used. Before measurement, samples were placed in the pan and crimped. The peak temperature of endotherms was considered as the melting temperature. Tg values were determined at half the height of the displacement.

5. Confocal microscopy

Fluorescent dyes, as stated in Sec. II B, were used to observe core–sheath fibers using a confocal laser scanning microscope (CLSM) (Zeiss LSM700). A 20× oil-immersion objective in a CLSM was used to observe the fluorescence of the fibers. The excitation wavelength was adjusted to 500–540 nm in sheath samples, while the emission wavelength was tuned to 488 nm. Thus, the excitation and emission wavelengths were set to 358 and 461 nm for core fiber samples. Z-stack pictures of fibers were captured from top to bottom with a slice thickness of 2.5 μm and a depth of ∼50 μm.

III. RESULTS AND DISCUSSION

A. Physical properties of solutions

In PG, solution viscosity and surface tension are the main parameters determining whether or not the fiber will be formed and the size and morphology of fibers.[39] Optimized viscosity and surface tension should be used to produce beadless and homogenous fibers. Also, fiber generation will not be achieved with solutions whose physical properties are outside the appropriate limits. For instance, higher than appropriate limits for surface tension generates heavily beaded fibers, and the opposite condition will cause fiber stretching.[40] Similarly, greater diameter fibers will be generated for higher viscosity; and fibers will not be formed at lower viscosity.[41]

PVA, PLA, and PCL solutions were dissolved at 20% (w/v), and PEO was dissolved at 10% (w/v) in their solvents. The polymer solutions' surface tensions were 62.1, 54.4, 28.1, and 156.4 m Nm^{-1}; their viscosities were 71.4, 153.2, 16.5, and 270 mPa s, respectively. The highest viscosity and surface tension belongs to the PEO solution, and the lowest values belong to the PCL solution, clearly the solvent used, polymer molecular weight and polymer concentration plays an anomalous role. All solutions were within appropriate limits with regard to surface tension, viscosity, and density to produce nonbeaded and homogenous core–sheath nanofibers (Fig. S1, supplementary material).

B. The core–sheath jetting behavior

This study captured high-speed camera videos to observe the core, sheath, and core–sheath polymer solutions' fluid behavior in CS

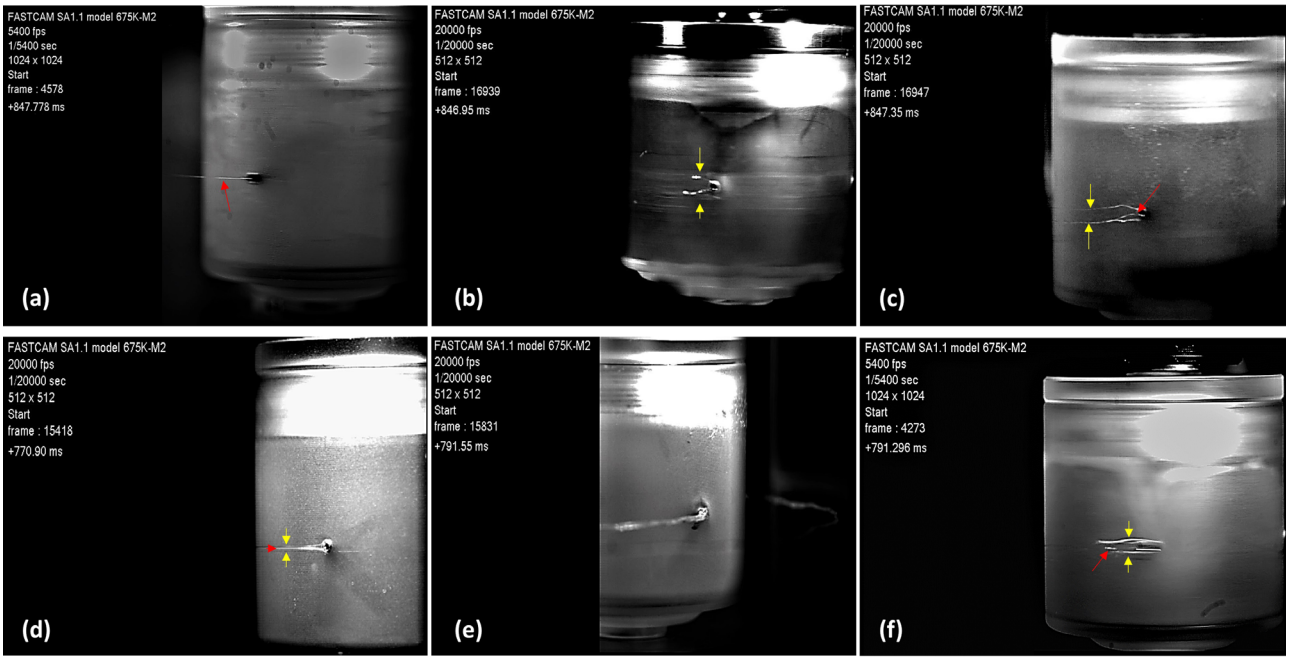

FIG. 3. Still pictures obtained from high-speed camera videos (which are given as video SV1-6, supplementary material): PEO solution at $\omega = 6000$ rpm as (a) core only, (b) sheath only, (c) core–sheath no pressure, (d) core–sheath with 0.1 MPa, (e) core–sheath with 0.2 MPa, and (f) core–sheath with 0.3 MPa pressure applied. (Red arrow corresponds to the core and yellow arrow corresponds to the sheath.)

and PG scenarios, as shown in Fig. 3. The core polymer solution jetted at 6000 rpm in CS as optimum speed since there were no fibers produced below this speed and solution was not jetted from all the core reservoir openings, due to lack of pressure [Fig. 3(a)]. In Fig. 3(b), only the sheath solution was loaded, and it is clearly shown that the jetted sheath solution flowed out from the top and the bottom of the sheath orifice to upward and downward streams away from the core. Core–sheath dual solutions in the CS scenario are illustrated in Fig. 3(c) and it is clearly shown that the core solution trajectory (forward) is in the same direction of the core opening, which touches the downstream of the sheath solution, whereas the upper stream of the sheath separates away from the core solution. In the PG scenario as shown in Fig. 3(d), optimum speed of 6000 rpm and 0.1 MPa pressure were applied; the trajectory of the jetted liquids from the core and the sheath accompanied each other since they jetted from their openings at the left bottom side of the sheath orifice. In Fig. 3(e), the spinning speed was kept constant at 6000 rpm, whereas the pressure increased to 0.2 MPa, and it is clearly shown that the sheath solution covered the core entirely during the process and the trajectory of the core–sheath dual solution appeared at the same time from the other openings. Finally, increasing the applied pressure to 0.3 MPa at constant speed led to turbulence behavior of the jetted liquids and this prevented the core and the sheath solutions from meeting, as shown in Fig. 3(f).

C. Numerical analysis

Effects of spinning speed at 6000 rpm without gas pressure in core–sheath reservoirs are illustrated in Fig. 4(a), and the polymer solution in the core reservoir could not reach the nozzle opening. In contrast, the sheath solution arrived at the orifices and jetted from the bottom side of the perforations, causing waste of polymer solution. Figure 4(b) shows that the polymer solutions of both core and sheath reach the orifices and the fluid in the sheath side moves to the topside of the chamber and the jetted fluid was not stable in this scenario. This phenomenon was studied in previous work for single-layer fiber production using CS.[27]

The jetted polymer solutions from the core–sheath reservoirs in the PG process were examined in this study; the optimum spinning speed and applied pressure were used as 6000 rpm and 0.2 MPa, respectively. As shown in Fig. 4(c), the gas pressure applied in the chamber increases both of the polymer solutions in both the core and sheath reservoirs to reach the openings at the same time, and they have almost the same profile, leading to jetting of the solutions to the atmosphere and fibers begin to be generated from all the orifices. The core container is illustrated in Fig. 4(d); the symmetrical profile of the fluids at the wall side of the nozzle openings is clearly shown from the top-side view of the chamber. From a close-up view of the inside of the hollow nozzles, it can be seen that PEO solution jetted at the side locations. In contrast, the top-side view of the sheath container illustrated in Fig. 4(e) shows the exact profile in the core container. Here, the jetted sheath solution at both sides of the orifice moves in the direction of the core fluid. Figure 4(f) gives an overview of how both the core and sheath fluids behave in their reservoirs, and it is clearly seen that the two polymer solutions moved simultaneously and jetted out together. A close view of the profile of the jetted core–sheath solutions, Fig. 4(g), shows clearly that the core polymer solution jetted out while the sheath solution surrounds both sides.

D. Morphology and size distribution of core–sheath fibers

1. Scanning electron microscopy

Although this study focuses on the internal morphology of nanofibers due to their core–sheath structure, external morphology and fiber diameter are also important in the characterization of nanofibers.[42] For example, in biomedical engineering applications, critical features such as drug release behavior, encapsulation efficiency, dissolution rate, degradation and swelling ratio, tensile properties, and cell proliferation can be altered by external morphology and fiber diameter.[43,44]

The smallest diameters were obtained with the samples in which PLA was the sheath. The diameter of PEO/PLA was measured as 529 ± 198 nm [Fig. 5(a)], PVA/PLA had 542.0 ± 165 nm [Fig. 5(b)]. As sheath, PLA nanofibers have a smaller diameter than PCL. In the case of water-soluble polymers as core, these values were PEO/PCL $= 740 \pm 225$ nm [Fig. 5(c)] and PVA/PCL $= 743 \pm 384$ nm [Fig. 5(d)]. In comparing PEO and PVA covered with PLA and PCL, nanofibers produced with PEO had a smaller diameter than PVA. The largest diameter was seen with PLA/PCL core–sheath nanofibers (875 ± 278) [Fig. 5(e)]. The most nonhomogeneous distribution of fiber was obtained with PVA/PCL core–sheath nanofibers.

2. Confocal fluorescence imaging

The confocal microscopy images illustrated in Fig. 6 confirmed that the vessel efficiently manufactures core–sheath fibers from water-soluble and water-insoluble polymers. Figure 6(a) illustrates the PEO as core in red color, and the sheath in green is PCL and is uniformly distributed as confirmed by the merged image when the core and the sheath are combined. Figure 6(b) shows the core (PVA) and the sheath (PCL) and the merged image confirmed that the sheath is entirely covered by the core. In Fig. 6(c), the PEO core is depicted in red, and the PLA sheath in green, confirming that the sheath distribution of PLA on PEO occurred as intended. Figure 6(d) confirms that the core (PVA) and sheath (PLA) layers were placed as intended and uniformly. Finally, using nonwater-soluble polymers as core (PLA) and as sheath (PCL) gives clear evidence that the core fibers are fully covered by the sheath, as shown in the merged image in Fig. 6(e). All the results provide strong evidence that the proposed vessel is capable of manufacturing the core–sheath with a uniform distribution.

3. Focused ion beam imaging

Figure 7 illustrates the cross-sectional view of core–sheath samples. Figure 7(a) shows PEO as a core and PCL as a sheath by specifically selecting a single coarse fiber as explained under experimental details in Sec. II G 2; the thickness of the sheath layer is $\sim 0.25\ \mu$m while the core diameter is approximately $8.0\ \mu$m. Figure 7(b) shows the PVA as a core and PCL as a sheath with thicknesses of 0.74and $15.4\ \mu$m, respectively. The third sample having PEO as a core and PLA as a sheath is illustrated in Fig. 7(c) and it clearly shows the core layer with a thickness of $\sim 0.13\ \mu$m and the layer thickness of the sheath is $\sim 1.98\ \mu$m. When PVA was chosen as a core and PLA as a sheath, the core diameter is $\sim 2.35\ \mu$m, whereas the sheath thickness is $\sim 0.2\ \mu$m as illustrated in Fig. 7(d). Finally, as shown in Fig. 7(e), the PLA core fiber diameter is $\sim 2.98\ \mu$m, and the accompanying sheath layer

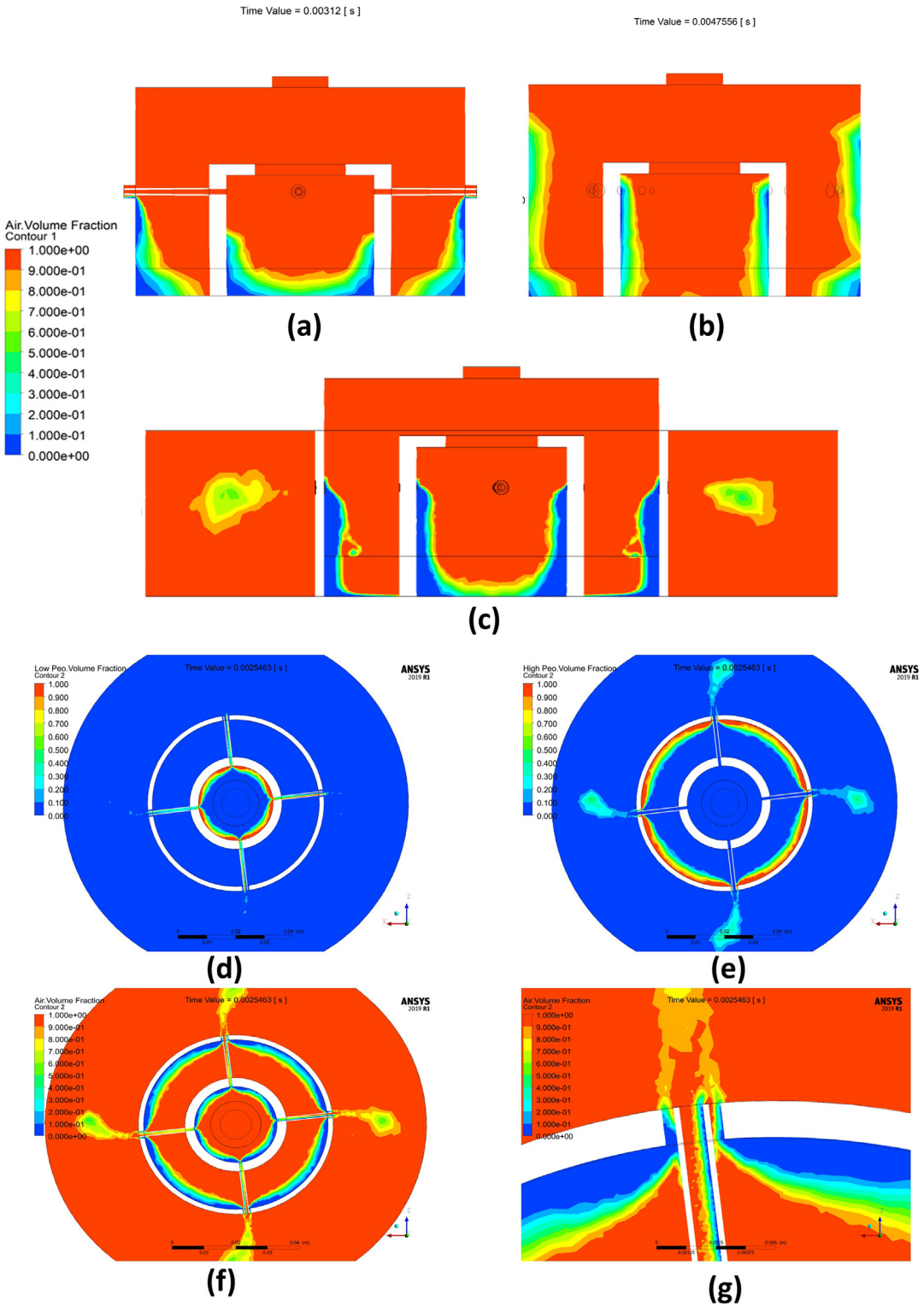

FIG. 4. Contours of the PEO solution in core–sheath containers at $\omega = 6000$ rpm (which are given as video SV7-10, supplementary material): (a) at t = 0.312 ms and (b) at t = 4.7556 ms no pressure applied, (c) with applied pressure ($P = 0.2$ MPa) at t = 2.5463 ms; (d) top-side view of core reservoir, (e) top-side view of sheath reservoir of (d) and (e) enable observation of the fluids in both reservoirs, separately; (f) top-side view for the core–sheath chamber; and (g) close-up view of the core–sheath outlet orifices.

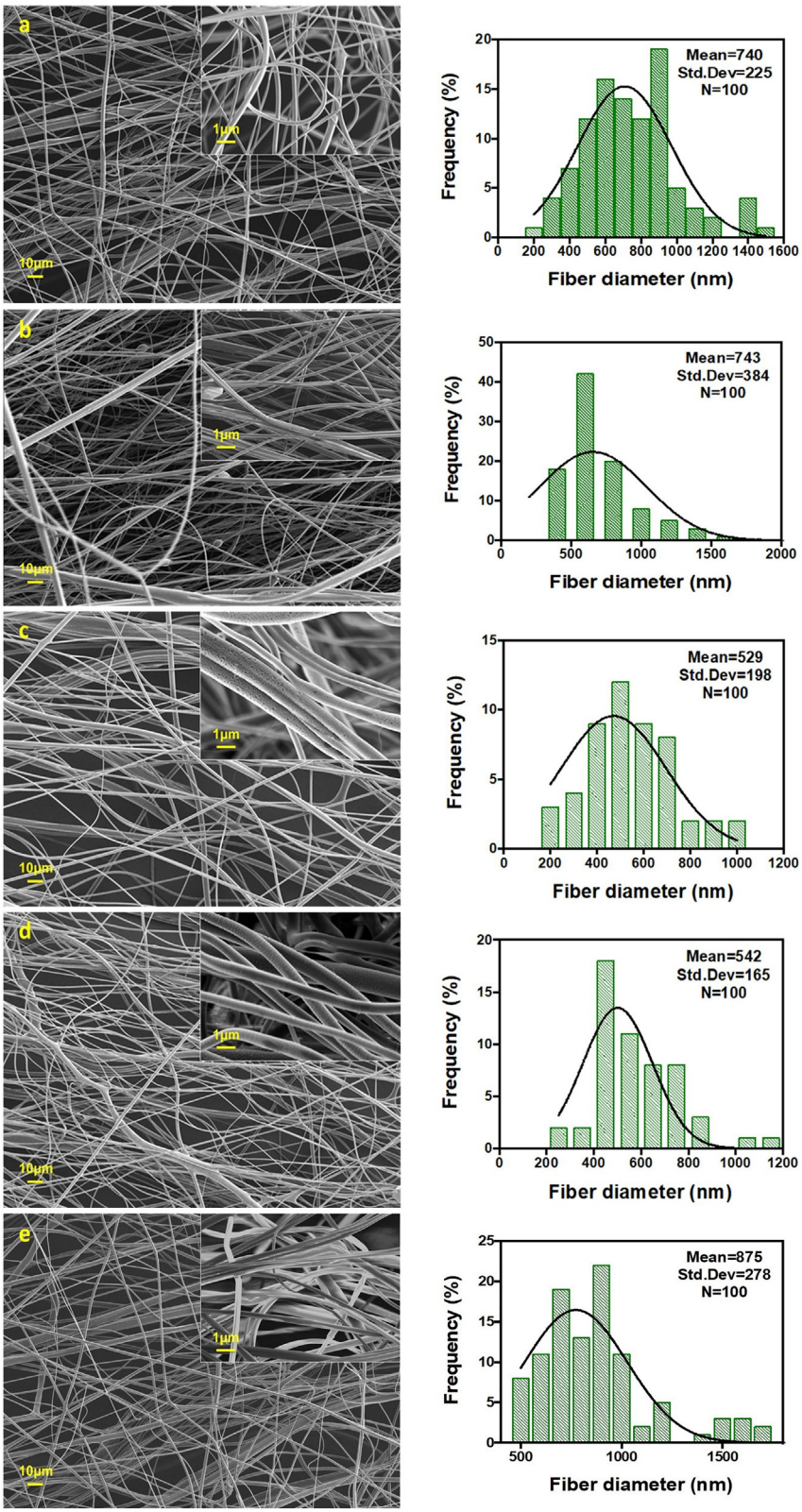

FIG. 5. SEM images and most representative fiber diameter distributions of core–sheath nanofibers produced by PG at 6000 rpm with 0.2 MPa pressure: (a) PEO/PCL, (b) PVA/PCL, (c) PEO/PLA, (d) PVA/PLA, (e) PLA/PCL. In all diameter distributions, n = 100.

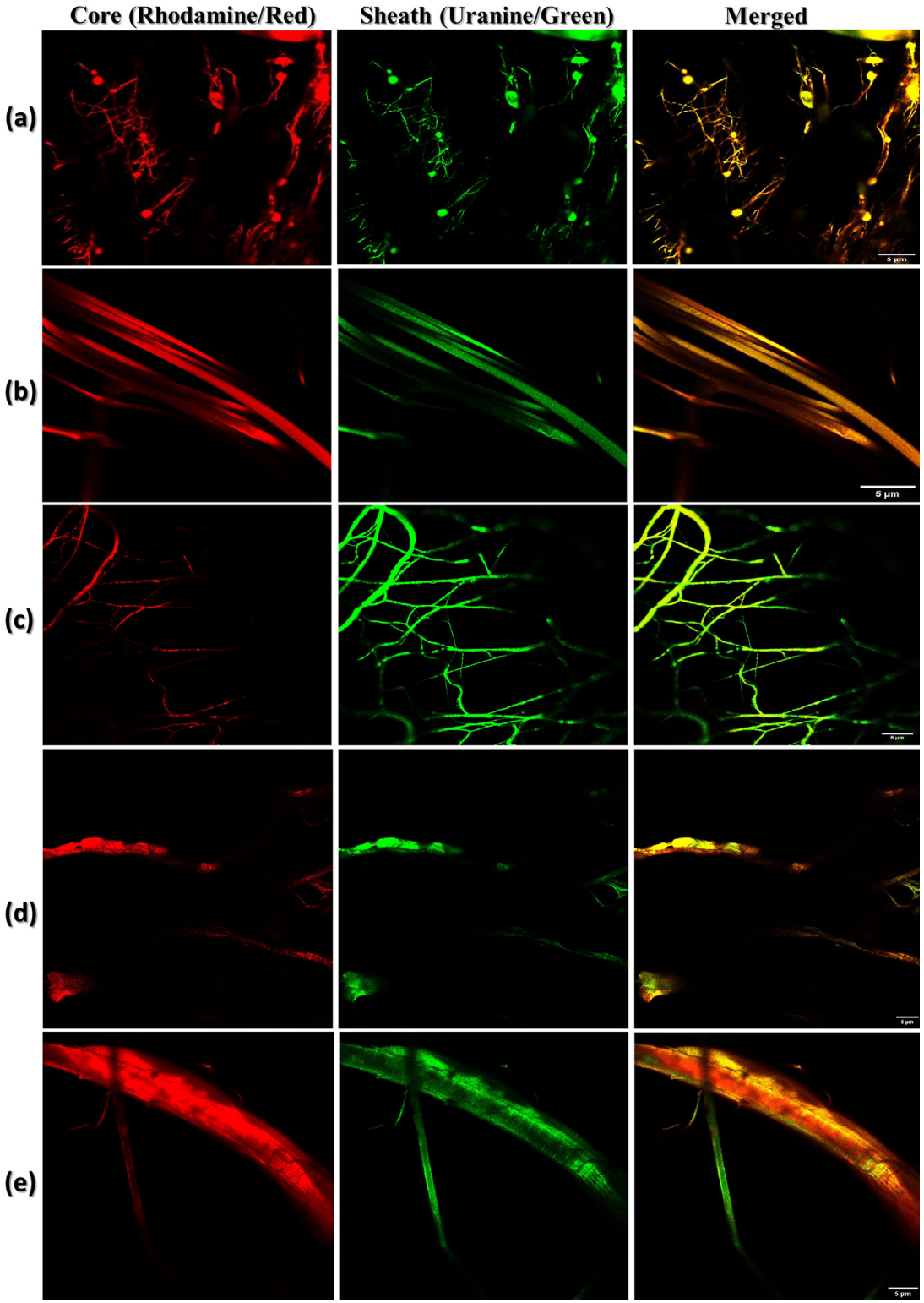

FIG. 6. Confocal laser scanning microscopy images of core–sheath nanofibers, Rhodamine (red) and Uranine (green) are used for the visualization of core and sheath fibers, respectively: (a) PEO/PCL, (b) PVA/PCL, (c) PEO/PLA, (d) PVA/PLA, and (e) PLA/PCL.

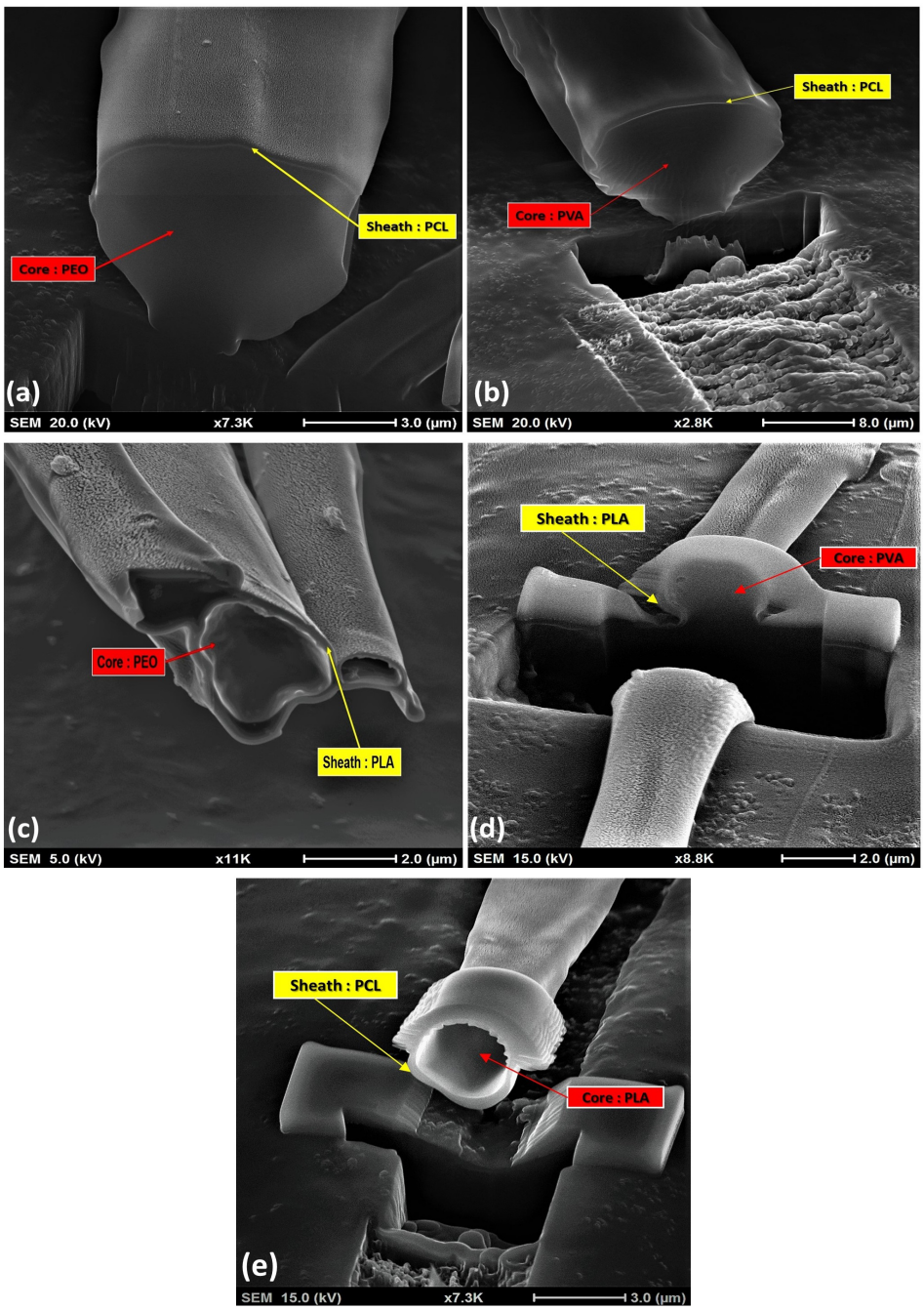

FIG. 7. FIB-SEM cross-sectional images of core/sheath fibers: (a) PEO/PCL, (b) PVA/PCL, (c) PEO/PLA, (d) PVA/PLA, and (e) PLA/PCL.

thickness is ∼0.31 μm. The FIB investigation, though not specifically on nanofibers, showed that the vessel delivers core–sheath fibers. More importantly, it shows that the (functional) sheath layer is much thinner compared to the core, and this is very economical as desired functional additions can be very expensive. In these investigations, we benefited from the fact that the fiber distributions (see Fig. 5) contained some coarser fibers. FIB is a difficult operation in core–sheath fibers where different thermal properties of the core and the sheath (different polymers) hinder the interpretation of results, especially in the case of nanofibers. Thus, to avoid unclear or distorted cross-sectional morphology or damage to the samples of core–sheath fibers,[45–47] we searched and located larger diameter fibers for FIB preparations as explained under experimental details in Sec. II G 2.

4. Fourier transform infrared spectroscopy (FTIR)

FTIR was utilized to prove the existence of intended materials in fibers, characterize functional groups, and differentiate prospective chemical changes between phases. The FTIR spectra of pure PVA, PEO, PLA, PCL, and core–sheath nanofibers were measured at a wavelength of 400–4000 cm^{-1} as shown in (Fig. 8). The C–O–C stretching vibration of PEO was observed at 1162.9 cm^{-1}, and these

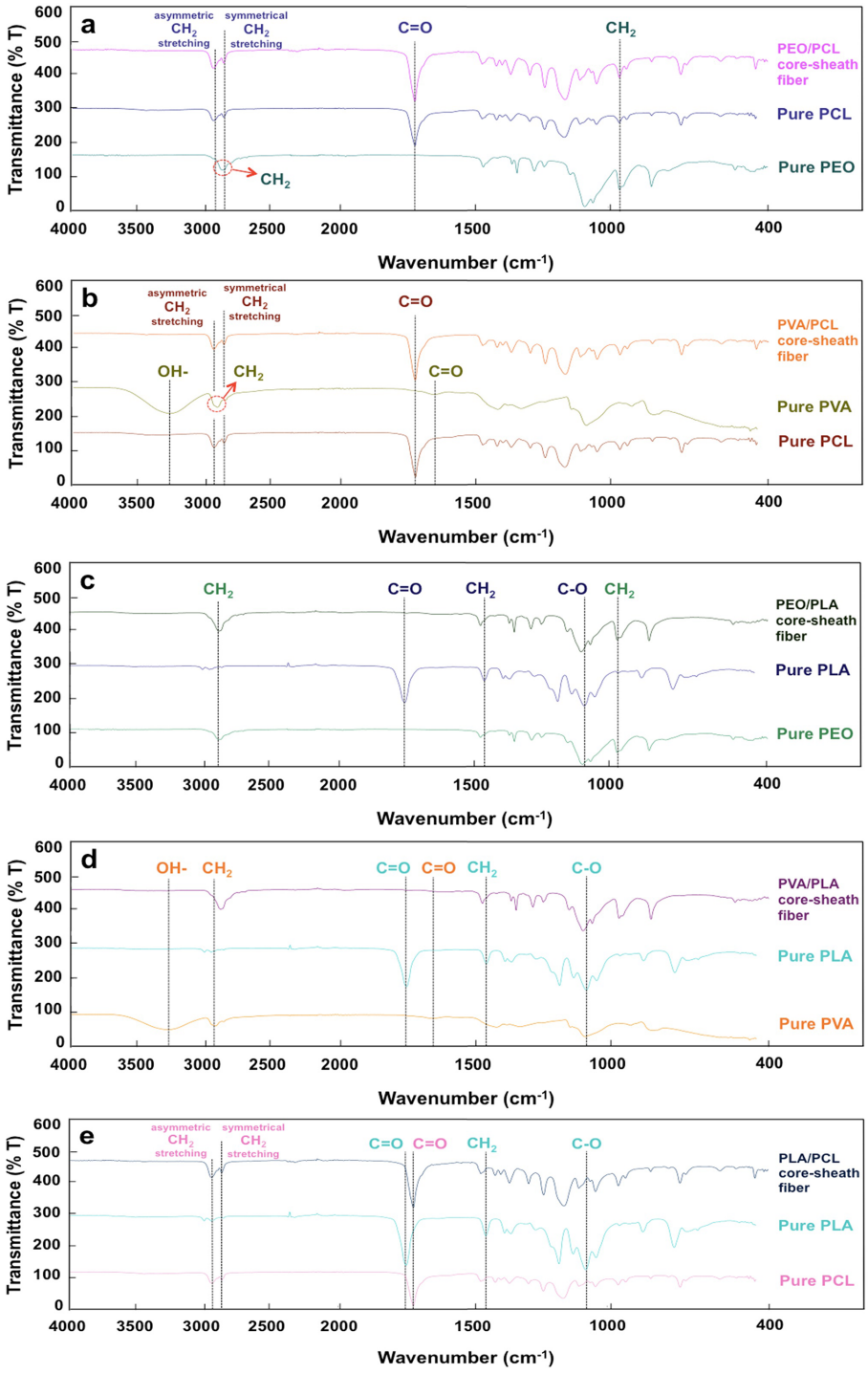

FIG. 8. FTIR spectra of PEO/PCL (a), PVA/PCL (b), PEO/PLA (c), PVA/PLA (d), and (e) PLA/PCL core–sheath nanofibers.

peaks are attributed to the amorphous content of PEO. A specific peak at 2865.7 cm^{-1} belongs to the asymmetric –C–H– stretching of CH_2 in the PEO spectrum.[48] Three peaks at 3268.9, 2914.8, and 1686.2 cm^{-1} correspond to the hydroxyl group, CH_2 asymmetric stretching, and C=O stretch, which is specific for the keto tautomer of PVA, respectively.[49] The characteristic peaks of PCL were seen at 2944.5 cm^{-1} (asymmetric CH_2 stretching), 2868.4 cm^{-1} (symmetrical CH_2 stretching), 1720.3 cm^{-1} (C=O stretching vibration), 1296.2 cm^{-1} (C–C and C–O stretching vibration), 1241.7 cm^{-1} (asymmetrical C–O–C– stretching vibration), and 1164.4 cm^{-1} (C=O–C stretching vibration).[50] In the PLA spectrum, C=O ester carbonyl groups at 1751.4 cm^{-1}, C–H deformation at 1457.4 and 1358.3 cm^{-1},

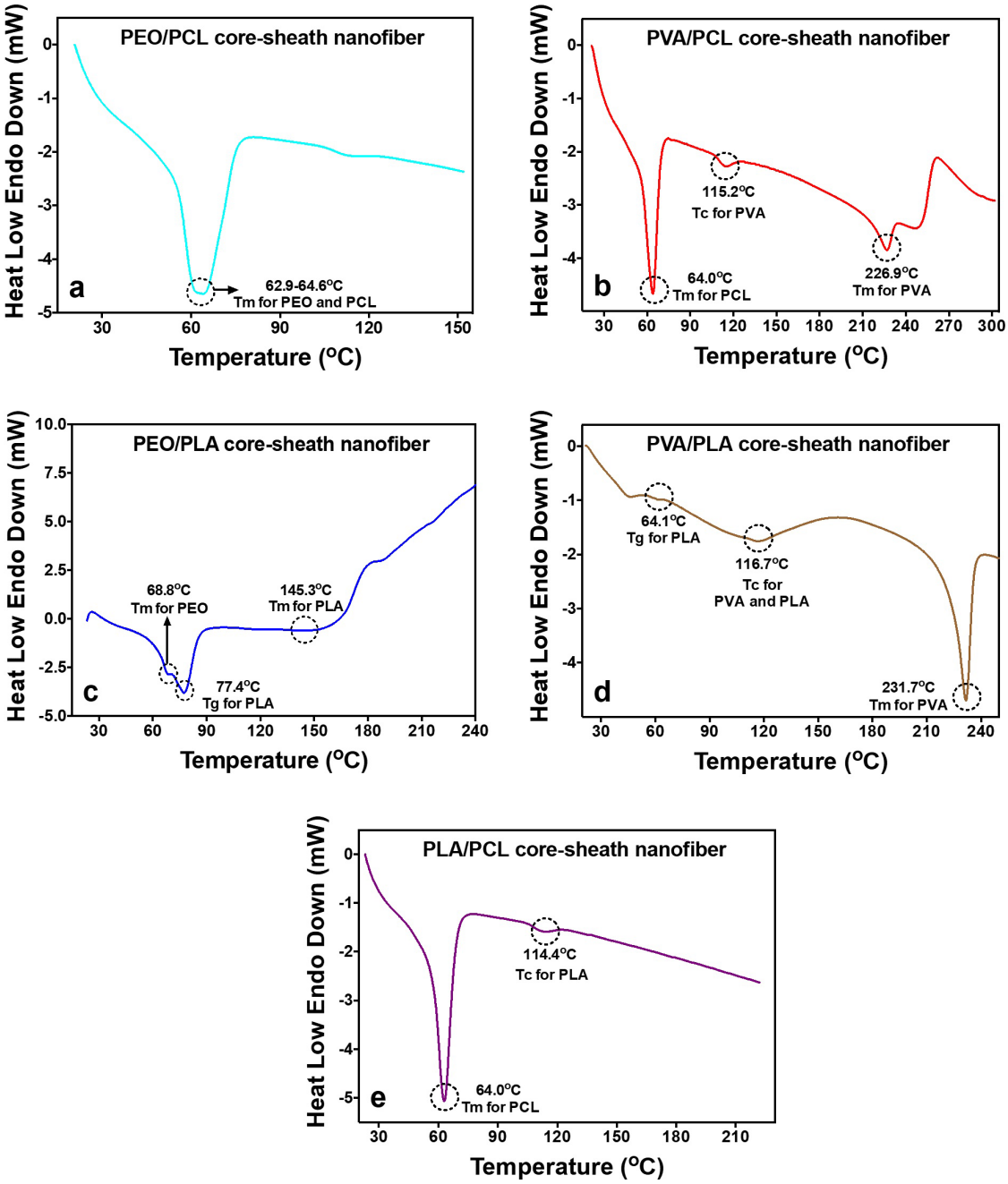

FIG. 9. DSC curves of the PEO/PCL (a), PVA/PCL (b), PEO/PLA (c), PVA/PLA (d), and PLA/PCL (e) core–sheath nanofibers. Tg: glass transition temperature, Tc: crystallization temperature, and Tm: melting temperature.

C–O stretching at 1180.1 and 1081.2 cm^{-1}, and C–C stretching at 869.8 cm^{-1} were detected.[51] PCL and PLA are aliphatic polymers with an analogous structure.

5. DSC analysis

DSC analysis is performed to detect the effect of the production technique on the thermal structure of core–sheath nanofiber samples. Crucial thermal parameters such as glass transition (Tg), cold crystallization (Tc), and melting temperatures (Tm) were measured between 0 and 300 °C for all samples, and the results are given in Fig. 9. According to the results, producing core–sheath nanofibers by PG causes slight changes in the thermal behavior of the polymers. In the PEO/PCL sample, Tm values for PEO and PCL are between 62.9 and 64.6 °C, as expected [Fig. 9(a)].[31,52] In the PVA/PCL sample, Tc and Tm points of PVA were seen at 115.2 °C and 226.9 °C, respectively.[53] There was no change in the Tm value of PCL (64.0 °C) [Fig. 9(b)]. The other sample investigated is PEO/PLA; it has higher Tg and lower Tm temperatures, which are 77.4 and 145.3 °C, respectively, than native PLA (63.0 and 164.0 °C), which could be due to the slightly lower crystallinity and increased free volume of the PLA chains caused by PG.[39] The Tm value of PEO is not changed (68.8 °C) [Fig. 9(c)]. In the PVA/PLA sample, the Tg value for PLA is observed at 64.1 °C, the Tc value for PVA and PLA is seen at around 116.7 °C, and the Tm for PVA is detected at 231.7 °C [Fig. 9(d)]. The Tm of PLA could not be detected in PVA/PLA and PLA/PCL samples. The Tm for PCL (64.0 °C) has not changed, and only the Tc point (114.4 °C) is seen for PLA in PLA/PCL samples [Fig. 9(e)].

IV. CONCLUSIONS AND FUTURE

In this research, a novel purpose-designed vessel was designed, constructed, and used to mass-produce core–sheath polymeric nanofibers. Both water-soluble and water-insoluble polymers were used. Furthermore, the fluid behavior within the core–sheath chamber was investigated using computational fluid dynamics, and the vessel's efficiency was proved. The pressureless process was optimal at 6000 rpm but caused depletion of the polymer solution before fiber generation. When pressure was used (PG method), core–sheath fibers were generated at 6000 rpm with 0.2 MPa optimum. The applied pressure supplies the solutions to be jetted more quickly to all orifices. Relative humidity (RH) plays a vital role in fabricating the fibers; the best RH was found at 46% ± 2% when all the other parameters were kept constant at ambient temperature. Furthermore, an experimental investigation was conducted using high-speed camera imaging to investigate the fluid behavior for the core–sheath jetted solutions to optimize to the best scenario; gas pressure at 0.2 MPa with 6000 rpm spinning speed allowed the sheath solution to cover the core entirely during the process. In contrast, it was observed that using no gas pressure or increasing the pressure to 0.3 MPa while maintaining the speed constant caused turbulence and prevented the core and sheath solutions from connecting. Meanwhile, the samples with PLA as the sheath and PEO and PVA as the core had the smallest fiber diameters (529 and 542 nm, respectively). Advanced microscopical characterization techniques proved that the sheath surrounded the core of the fibers uniformly distributed, achieving the desired thin sheath on the core. Spectroscopy confirmed that core–sheath nanofibers of the intended polymeric compositions were successfully produced. Calorimetry measurements showed that the polymeric constituents did not suffer noteworthy degradation due to the forming technology. The results found in this research have led to a firm foundation for ongoing and future research, to proceed to the manufacturing of multi-layer (≥2) polymeric fibers using a fully automated vessel and system, to simultaneously control polymer solution flow rates, spinning speed, applied pressure, temperature, humidity, and collector distance for each layer. We are also attempting to set controls that will allow the achievement of near-monodisperse fiber diameter distributions at a selected scale (e.g., micro or nano).

SUPPLEMENTARY MATERIAL

See the supplementary material for further details about videos extracted from a high-speed camera recording of only core solution behavior using the centrifugal spinning (CS) technique at 6000 rpm without applied pressure (supplementary material Video 1), only sheath (supplementary material Video 2), and core–sheath (supplementary material Video 3). The videos extracted from a high-speed camera during the use of the pressurized gyration technique (PG) for only the core-sheath solution at 6000 rpm and at 0.1 MPa (supplementary material Video 4), 0.2 MPa (supplementary material Video 5), and 0.3 MPa (supplementary material Video 6) are provided. Additionally, videos obtained from CFD software recording of core–sheath fluid behavior in the CS technique at 6000 rpm (supplementary material Videos 7 and 8), as well as core–sheath fluid behavior in the PG method at 6000 rpm and at 0.2 MPa (supplementary material Videos 9 and 10) are included.

ACKNOWLEDGMENTS

The authors are grateful to the U.K. Engineering & Physical Sciences Research Council (EPSRC) for funding pressurized gyration forming research at University College London (Grant Nos. EP/L023059/1, EP/N034228/1, and EP/S016872/1). In addition, the authors would like to express deep gratitude to PAAET-Kuwait for funding Alenezi's Ph.D. study (Grant No. 278010301647). Finally, we would also like to thank Mehmet Ezer from Tribot, Turkey, for his assistance in constructing the device.

AUTHOR DECLARATIONS

Conflict of Interest

The authors have no conflicts to disclose.

REFERENCES

[1]Q. Pham Le, M. V. Uspenskaya, R. O. Olekhnovich, and M. A. Baranov, Fibers **9**(1), 2 (2021).
[2]J. Jeevanandam, A. Barhoum, Y. S. Chan, A. Dufresne, and M. K. Danquah, Beilstein J. Nanotechnol. **9**, 1050–1074 (2018).
[3]A.-T. Iacob, M. Drăgan, O.-M. Ionescu, L. Profire, A. Ficai, E. Andronescu, L. G. Confederat, and D. Lupaşcu, Pharmaceutics **12**(10), 983 (2020).
[4]E. A. Kamoun, X. Chen, M. S. Mohy Eldin, and E.-R. S. Kenawy, Arabian J. Chem. **8**(1), 1–14 (2015).
[5]E. M. Elmowafy, M. Tiboni, and M. E. Soliman, J. Pharm. Invest. **49**(4), 347–380 (2019).
[6]H. O. Paipa-Álvarez, W. Palacios Alvarado, and B. Medina Delgado, J. Phys. **1672**, 012013 (2020).
[7]M. Cai, H. He, X. Zhang, X. Yan, J. Li, F. Chen, D. Yuan, and X. Ning, Nanomaterials **9**(1), 39 (2019).
[8]Z. Gu, H. Yin, J. Wang, L. Ma, Y. Morsi, and X. Mo, Colloids Surf. B **161**, 331–338 (2018).

[9]D. Han and A. J. Steckl, ACS Appl. Mater. Interfaces **9**(49), 42653–42660 (2017).
[10]F. Zamani, M. Amani-Tehran, M. Latifi, M. A. Shokrgozar, and A. Zaminy, J. Biomed. Mater. Res. Part A **102**(2), 506–513 (2014).
[11]Y. Wang, Z. Li, P. Shao, S. Hao, W. Wang, Q. Yang, and B. Wang, Mater. Sci. Eng.: C **44**, 109–116 (2014).
[12]M. Naeimirad, A. Zadhoush, R. Kotek, R. E. Neisiany, S. Nouri Khorasani, and S. Ramakrishna, J. Appl. Polym. Sci. **135**(21), 46265 (2018).
[13]X. Yan, J. Marini, R. Mulligan, A. Deleault, U. Sharma, M. P. Brenner, G. C. Rutledge, T. Freyman, and Q. P. Pham, PLoS One **10**(5), e0125407 (2015).
[14]M. Dasdemir, B. Maze, N. Anantharamaiah, and B. Pourdeyhimi, J. Mater. Sci. **47**(16), 5955–5969 (2012).
[15]S. Bairagi and S. W. Ali, Eur. Polym. J. **116**, 554–561 (2019).
[16]G. Mourgas, E. Giebel, T. Schneck, J. Unold, and M. R. Buchmeiser, J. Appl. Polym. Sci. **136**(31), 47829 (2019).
[17]A. L. Yarin, S. Koombhongse, and D. H. Reneker, J. Appl. Phys. **90**(9), 4836–4846 (2001).
[18]J. Hong, M. Yeo, G. H. Yang, and G. Kim, Int. J. Mol. Sci. **20**(24), 6208 (2019).
[19]S. Mahalingam and M. Edirisinghe, Macromol. Rapid Commun. **34**(14), 1134–1139 (2013).
[20]P. L. Heseltine, J. Ahmed, and M. Edirisinghe, Macromol. Mater. Eng. **303**(9), 1800218 (2018).
[21]S. Padron, A. Fuentes, D. Caruntu, and K. Lozano, J. Appl. Phys. **113**(2), 024318 (2013).
[22]X. Xu and J. Luo, Appl. Phys. Lett. **91**(12), 124102 (2007).
[23]B. T. Raimi-Abraham, S. Mahalingam, M. Edirisinghe, and D. Q. Craig, Mater. Sci. Eng.: C **39**, 168–176 (2014).
[24]P. Mellado, H. A. McIlwee, M. R. Badrossamay, J. A. Goss, L. Mahadevan, and K. K. Parker, Appl. Phys. Lett. **99**(20), 203107 (2011).
[25]J. N. r So/rensen and E. A. Christensen, Phys. Fluids **7**(4), 764–778 (1995).
[26]J. J. Rogalski, L. Botto, C. W. M. Bastiaansen, and T. Peijs, J. Appl. Polym. Sci. **137**(33), 48963 (2020).
[27]H. Alenezi, M. E. Cam, and M. Edirisinghe, Appl. Phys. Rev. **6**(4), 041401 (2019).
[28]A. R. Hashemi, A. R. Pishevar, A. Valipouri, and E. I. Părău, Phys. Fluids **30**(1), 017103 (2018).
[29]S. Mahalingam, R. Matharu, S. Homer-Vanniasinkam, and M. Edirisinghe, Appl. Phys. Rev. **7**(4), 041302 (2020).
[30]S. Rafiei, B. Noroozi, L. Heltai, and A. K. Haghi, J. Ind. Text. **47**(7), 1791–1811 (2018).
[31]E. Araneda, A. Leiva, L. Gargallo, N. Hadjichristidis, I. Mondragon, and D. Radic, Polym. Eng. Sci. **52**(5), 1128–1136 (2012).
[32]S. Mahalingam, S. Homer-Vanniasinkam, and M. Edirisinghe, Mater. Des. **178**, 107846 (2019).
[33]S. Mahalingam, S. Huo, S. Homer-Vanniasinkam, and M. Edirisinghe, Polymers **12**(8), 1709 (2020).
[34]S. Mahalingam, C. Bayram, M. Gultekinoglu, K. Ulubayram, S. Homer-Vanniasinkam, and M. Edirisinghe, Macromol. Biosci. **21**(10), 2100177 (2021).
[35]Y. Lei, Y. Li, S. Jing, C. Song, Y. Lyu, and F. Wang, Appl. Therm. Eng. **125**, 870–879 (2017).
[36]W. Szablewski, ZAMM-J. Appl. Math. Mech./Z. Angew. Math. Mech. **53**(6), 424–424 (1973).
[37]B. E. Launder and D. B. Spalding, Comput. Methods Appl. Mech. Eng. **3**(2), 269–289 (1974).
[38]T.-H. Shih, W. W. Liou, A. Shabbir, Z. Yang, and J. Zhu, Comput. Fluids **24**(3), 227–238 (1995).
[39]M. E. Cam, A. N. Hazar-Yavuz, S. Cesur, O. Ozkan, H. Alenezi, H. Turkoglu Sasmazel, M. Sayip Eroglu, F. Brako, J. Ahmed, L. Kabasakal, G. Ren, O. Gunduz, and M. Edirisinghe, Int. J. Pharm. **588**, 119782 (2020).
[40]R. T. Weitz, L. Harnau, S. Rauschenbach, M. Burghard, and K. Kern, Nano Lett. **8**(4), 1187–1191 (2008).
[41]M. E. Cam, S. Yildiz, H. Alenezi, S. Cesur, G. S. Ozcan, G. Erdemir, U. Edirisinghe, D. Akakin, D. S. Kuruca, L. Kabasakal, O. Gunduz, and M. Edirisinghe, J. R. Soc. Interfaces **17**(162), 20190712 (2020).
[42]T. Roodbar Shojaei, A. Hajalilou, M. Tabatabaei, H. Mobli, and M. Aghbashlo, in *Handbook of Nanofibers*, edited by A. Barhoum, M. Bechelany, and A. S. H. Makhlouf (Springer International Publishing, Cham, 2019), pp. 491–522.
[43]M. E. Cam, B. Ertas, H. Alenezi, A. N. Hazar-Yavuz, S. Cesur, G. S. Ozcan, C. Ekentok, E. Guler, C. Katsakouli, Z. Demirbas, D. Akakin, M. S. Eroglu, L. Kabasakal, O. Gunduz, and M. Edirisinghe, Mater. Sci. Eng.: C **119**, 111586 (2021).
[44]J. Wu, Z. Zhang, J. G. Gu, W. Zhou, X. Liang, G. Zhou, C. C. Han, S. Xu, and Y. Liu, J. Controlled Release **320**, 337–346 (2020).
[45]S. Kim, M. Jeong Park, N. P. Balsara, G. Liu, and A. M. Minor, Ultramicroscopy **111**(3), 191–199 (2011).
[46]N. D. Bassim, B. T. De Gregorio, A. L. D. Kilcoyne, K. Scott, T. Chou, S. Wirick, G. Cody, and R. M. Stroud, J. Microsc. **245**(3), 288–301 (2012).
[47]K. C. Wong, C. M. Haslauer, N. Anantharamaiah, B. Pourdeyhimi, A. D. Batchelor, and D. P. Griffis, Microsc. Microanal. **16**(3), 282–290 (2010).
[48]C. Hu, R. Gong, and F. Zhou, Int. J. Polym. Sci. **2015**, 12.
[49]A. Kharazmi, N. Faraji, R. Mat Hussin, E. Saion, W. M. Yunus, and K. Behzad, Beilstein J. Nanotechnol. **6**, 529–536 (2015).
[50]R. Fang, E. Zhang, L. Xu, and S. Wei, J. Nanosci. Nanotechnol. **10**(11), 7747–7751 (2010).
[51]A. Alakrach, N. Noriman, O. S. Dahham, R. Hamzah, M. A. Alsaadi, Z. Shayfull, and S. S. Idrus, J. Phys. **1019**, 012065 (2018).
[52]P. Piyasin, R. Yensano, and S. Pinitsoontorn, Polymers **11**(11), 1768 (2019).
[53]D. Thomas, E. Zhuravlev, A. Wurm, C. Schick, and P. Cebe, Polymer **137**, 145–155 (2018).